THE JOURNAL OF PHYSICAL CHEMISTRY B

Article

Cite This: J. Phys. Chem. B 2018, 122, 8675−8684

pubs.acs.org/JPCB

Phenyl-Ring Dynamics in Amyloid Fibrils and Proteins: The Microscopic-Order-Macroscopic-Disorder Perspective

Eva Meirovitch,*[,†] Zhichun Liang,[‡] and Jack H. Freed[‡]

[†]The Mina and Everard Goodman Faculty of Life Sciences, Bar-Ilan University, Ramat-Gan 5290002, Israel

[‡]Baker Laboratory of Chemistry and Chemical Biology, Cornell University, Ithaca, New York 14853-1301, United States

Supporting Information

ABSTRACT: We have developed the microscopic-order-macroscopic-disorder (MOMD) approach for studying internal mobility in polycrystalline proteins with ^{2}H lineshape analysis. The motion itself is expressed by a diffusion tensor, $\boldsymbol{R}$, the local spatial restraints by a potential, u, and the "local geometry" by the relative orientation of the model-related and nuclear magnetic resonance-related tensors. Here, we apply MOMD to phenyl-ring dynamics in several Aβ_{40}-amyloid-fibrils, and the villin headpiece subdomain (HP36). Because the available data are limited in extent and sensitivity, we adjust u and $\boldsymbol{R}$ in the relevant parameter ranges, fixing the "local geometry" in accordance with standard stereochemistry. This yields a physically well-defined and consistent picture of phenyl-ring dynamics, enabling comparison between different systems. In the temperature range of 278−308 K, u has a strength of (1.7−1.8) kT and a rhombicity of (2.4−2.6) kT, and $\boldsymbol{R}$ has components of $5.0 \times 10^2 \leq R_\perp \leq 2.0 \times 10^3$ s^{-1} and $6.3 \times 10^5 \leq R_\parallel \leq 2.0 \times 10^6$ s^{-1}. At 278 K, fibril hydration increases the axiality of both u and $\boldsymbol{R}$; HP36 hydration has a similar effect at 295 K, reducing $R_\perp$ considerably. The D23N mutation slows down the motion of the probe; Aβ_{40} polymorphism affects both this motion and the related local potential. The present study identifies the impact of various factors on phenyl-ring mobility in amyloid fibrils and globular proteins; the difference between the two protein forms is considerable. The distinctive impact of hydration on phenyl-ring motion and previously studied methyl-group motion is also examined. The ^{2}H lineshapes considered here were analyzed previously with various multi-simple-mode (MSM) models, where several simple motional modes are combined. The MOMD and MSM interpretations differ in essence.

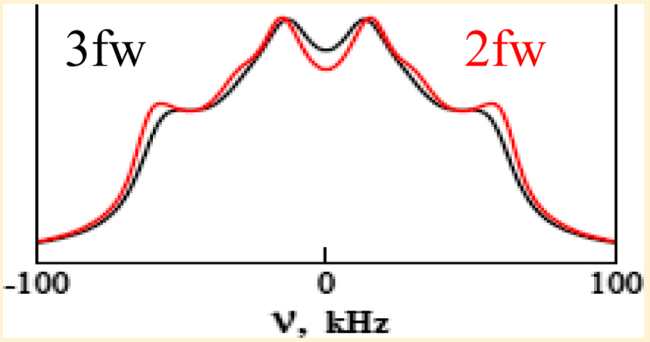

1. INTRODUCTION

Nuclear magnetic resonance (NMR) lineshape analysis is a powerful method for studying structural dynamics in the solid state.[1−6] The motions investigated are typically of the internal restricted type, reflecting molecular flexibility.[7−10] Deuterium is a particularly useful NMR nucleus in this context. The methyl-moiety, C−CD$_3$, and the methylene bond, C−D, were used in early work to obtain information on the flexibility of small organic molecules, peptides, and even proteins.[2,3,5,6] The dynamic models utilized consisted of relatively simple jump-type modes, adapted to each specific case studied.[1−6] Later on, more elaborate models, based on the solution of simple stochastic Liouville equations (SLEs), were developed.[11,12] However, except for a few simple cases, it was necessary to combine several simple dynamic modes, taken independently, in order to obtain good statistics in fitting the experimental data.[11−13] We call this the multi-simple-mode (MSM) method. Different authors conceive of different simple motions; hence, the MSM models are diverse, rendering comparison difficult. Improvement can only be accomplished by including yet another dynamic mode; this changes the overall MSM model. Independence of the individual modes is assumed but might not be valid.

No model can be proven to be unique. However, one can conceive of a consistent and reasonably general approach. The very anisotropic reorientation (VAR) model for treating internal motions in macromolecules was developed in early work.[14] VAR features a single diffusive motion about a tilted (in the magnetic tensor frame) internal axis. Among other probes, VAR was applied to deuterium.[15] This model is consistent but limited, as it ignores the local spatial restraints.

Recently, we developed the microscopic-order-macroscopic-disorder (MOMD) approach, originally formulated for ESR applications,[16] for the analysis of ^{2}H lineshapes from polycrystalline proteins and other molecules.[17−20] MOMD is based on the SLE developed by Freed and co-workers for treating locally restricted motions.[21,22] It is more general than the models noted above. All of the major factors—type of motion, spatial restraints, and local geometry—are treated for

Received: July 3, 2018
Revised: August 24, 2018
Published: August 24, 2018

DOI: 10.1021/acs.jpcb.8b06330
J. Phys. Chem. B 2018, 122, 8675−8684

the entire motional range within their rigorous three-dimensional tensorial requirements. The motion itself is expressed by a diffusion tensor, $\boldsymbol{R}$, and the spatial restraints by a (dimensionless) potential u. Rigorously, u is expanded in the full basis set of the Wigner rotation matrix elements. This expansion is truncated in accordance with the symmetry of the system and data sensitivity. One can "tailor'" u so that on the whole, a jump-type scenario emerges.[23] A local ordering tensor may be defined in terms of u;[22] thus, the local spatial restraints may be expressed in terms of order parameters, in addition to potential coefficients. The local geometry is given by the relative orientation of the model-related and NMR-related tensors. MOMD largely overcomes the MSM-related problems outlined above.

In the past, we applied MOMD to solid-state methyl-moiety and methylene dynamics.[17−20] Among others, we treated quite extensive and sensitive sets of ^{2}H lineshapes from the villin headpiece subdomain (HP36)[17] and several Aβ_{40}-amyloid-fibril variants.[20] All of these spectra had been analyzed previously with MSM models (cf. refs 17 and 20 for details). The current version of MOMD describes methyl dynamics in terms of an axial diffusion tensor, a rhombic potential, and adjustable features of local geometry.[17,20] MOMD and MSM yield different pictures of structural dynamics.[17,20]

In this study, we apply MOMD to phenyl-ring dynamics in the villin headpiece subdomain (HP36), and the same Aβ_{40}-amyloid-fibril variants studied previously within the scope of methyl dynamics. Compared with the methyl-moiety data we used previously,[17,20] the phenyl-ring data we are using currently[24,25] are (for practical reasons) considerably more limited in extent. In addition, as the actual values of the rate constants reside in parameter ranges close to the extremes of the time window (see below), data sensitivity is limited. These data were analyzed previously with MSM models.[24,25] The authors of refs 24 and 25 aimed at precise reproduction of the experimental lineshapes. To accomplish this, two (for the fibrils)[25] and three (for HP36)[24] dynamic modes were combined within the scope of various assumptions; distributions in the pertinent activation energies, E_a, constituted the essence of the interpretation; mean E_a values were used to parametrize the local potential.[25]

We devised an analysis strategy that takes into account data paucity and limited data sensitivity. Given these circumstances, the objective has been set to capture the key features of phenyl-ring dynamics and describe them in terms of the physically well-defined MOMD parameters. As shown below, this can be accomplished by reproducing the key features of the experimental ^{2}H lineshapes.

Internal phenyl- and tyrosyl-ring dynamics in proteins is a puzzling phenomenon. It was detected in early work and interpreted in terms of π-flips around the C$^\beta$−C$^\xi$ axis[26] (Figure 1). Such motion requires the transient creation of a large activated free volume in the tightly packed protein core. A recent study found that in ubiquitin, this motion is diffusive above 312 K.[27] Such motion does not require drastic structural changes in the protein core. It is likely to be quite general in nature; its belated detection[27] is probably related to preferences for multimode and/or multicomponent analyses when π-flips alone fail to reproduce the experimental data.[28−33]

In MOMD, the motion is inherently diffusive but with a restrictive potential. The local potential can be devised—by lowering its symmetry—so as to describe with reasonably good approximation compact protein-core environments.[16,17] In

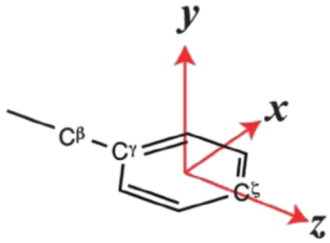

Figure 1. Phenyl-ring schematic; depicted are the principal axes of the motionally-averaged ^{2}H quadrupole tensor yielded by very fast π-flips around the C$^\beta$−C$^\xi$ axis.[48]

previous work, we developed strategies for ascertaining that the data analyzed are not over-interpreted.[34] Thus, MOMD is expected to be particularly useful for studying phenyl- and tyrosyl-ring dynamics in proteins.

The villin headpiece subdomain is a 35-residue autonomously folding motif comprising the extreme C-terminus of villin,[35] a F-actin bundling protein.[36] The structure of HP36 consists of three short helices surrounding a tightly packed hydrophobic core[37,38] (Figure 2). Better understanding the

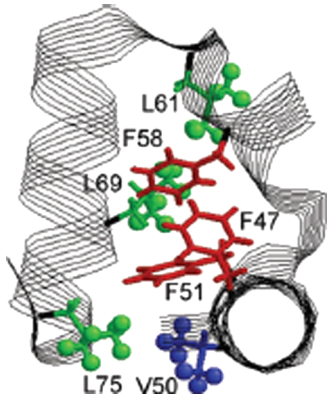

Figure 2. Ribbon diagram of the chicken villin headpiece subdomain (HP36).[25] The side-chains of the phenyl-ring-bearing residues F51 and F58, treated in this study, are depicted in red. The side-chains of the methyl-bearing residues L61, L69 and L75 (green), and V50 (purple), studied previously,[20] are depicted.

properties of the protein core, which plays a major role in protein stability, folding, and biological function, is important. The core of HP36 comprises the sidechains of residues F51 and F58, the aromatic rings of which were selectively deuterated.[24] The respective ^{2}H lineshapes, acquired at 295 K, were analyzed previously with an MSM model;[24] they are analyzed here with MOMD.

The Aβ_{40}-amyloid fibrils ("40" stands for the number of residues in the peptide) and associated aggregates are key molecular manifestations of the devastating Alzheimer's disease.[39−42] To aid in developing effective preventive and therapeutic agents, as yet unavailable, it is important to acquire better information on structural and dynamic properties of these fibrils. We study here hydrated 2-fold symmetric striated-ribbon (Figure 3a) and 3-fold symmetric twisted (Figure 3b) polymorphs of the wild-type (WT) Aβ_{40} peptide[43−45] and the protofibrils of its D23N mutant[46] (Figure 3c). The two former fibril variants are denoted 2fw and 3fw when hydrated and 2fd and 3fd when dry. The aromatic ring of the side chain of residue F19 in all three variants was selectively deuterated.[25]

DOI: 10.1021/acs.jpcb.8b06330
J. Phys. Chem. B 2018, 122, 8675−8684

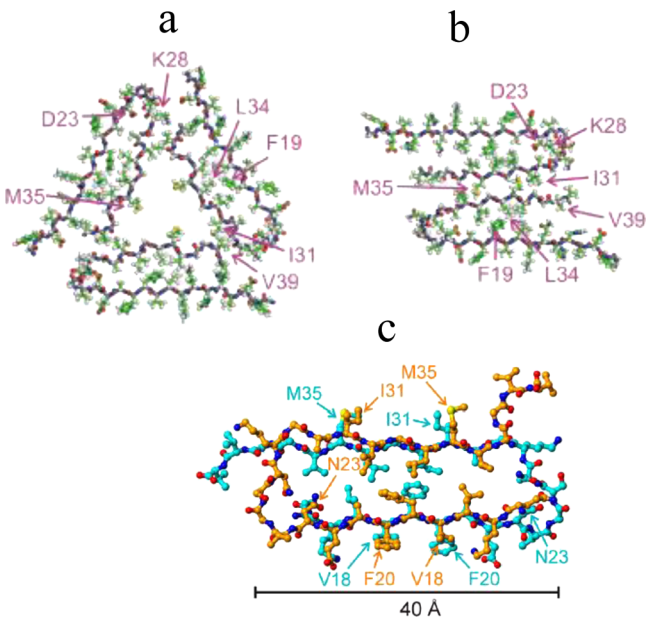

Figure 3. Atomic representations of the 3-fold-symmetric Aβ_{40} fibril (part a), and the 2-fold-symmetric fibril (part b), viewed down the fibril axis. Hydrophobic, polar, negatively-charged and positively-charged amino-acid side-chains are green, magenta, red and blue, respectively. Backbone nitrogen and carbonyl-oxygen atoms are cyan and pink, respectively. The unstructured N-terminal residues 1−8 are omitted.[45] Atomic representations of the protofibril of the D23N mutant viewed down the fibril axis. All the non-hydrogen atoms of residues 15−40 are depicted. The central-pair of a 4-pair-containing structure is shown (part c).[46]

^{2}H lineshapes, acquired at 278, 295, and 308 K, were analyzed previously with an MSM model;[25] they are analyzed here with MOMD.

Consistent MOMD analyses of structural dynamics are presented for all of the phenyl-ring systems studied, elucidating the impact of key factors. New information emerges from comparison of different systems, in particular between Aβ_{40} fibrils and HP36, and from connection with the previously derived MOMD picture of methyl-moiety dynamics.[20]

A theoretical summary is provided in section 2, results and discussion are presented in section 3, and our conclusions appear in section 4.

2. THEORETICAL SUMMARY

The MOMD theory as applied to NMR has been delineated previously.[17−20] For convenience, its basics are given below. Figure 4 shows the MOMD frame scheme for a deuterium nucleus. L is the space-fixed laboratory frame. C is the local director frame fixed in the molecule. M denotes the principal axis system (PAS) of the local ordering tensor, $\boldsymbol{S}$, taken the same (for simplicity) as the PAS of the local diffusion tensor, $\boldsymbol{R}$. Q denotes the PAS of the quadrupolar tensor. The M and Q frames are fixed in the probe.

The Euler angles Ω_{CM} (associated with the orientation and diffusion of the probe relative to the local director) are time-dependent. The Euler angles $\Omega_{MQ} = (\alpha_{MQ}, \beta_{MQ}, \gamma_{MQ})$ are time-independent. Given that the Q frame is axially symmetric, one has $\gamma_{MQ} = 0$. For simplicity, the angle α_{MQ} is set equal to zero. Thus, the orientation of Z_M (main ordering/diffusion axis) relative to Z_Q (the principal axis of the effective quadrupolar tensor) is given by the polar angle, β_{MQ}. Because there is no

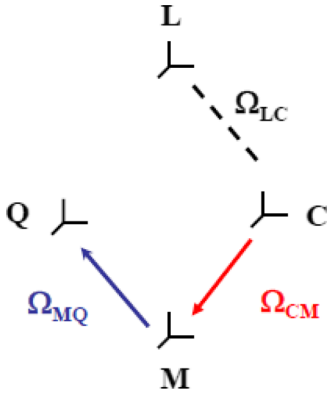

Figure 4. MOMD frames: L—lab frame, C—local director frame, M—local ordering/local diffusion frame, Q—quadrupolar tensor frame. The Euler angles depicted in red are time-dependent; the Euler angles depicted in blue are time-independent; the Euler angles depicted in black are distributed in space at random.

"macroscopic order", one has to calculate ^{2}H spectra for a large enough number of Ω_{LC} values and sum the emerging lineshapes according to a random distribution.[16,17]

The SLE for a rigid particle diffusing in anisotropic medium with director parallel to the external magnetic field is given by[21]

$$\left(\frac{\partial}{\partial t}\right)\rho(\Omega, t) = [-i\mathcal{H}(\Omega)^X - \Gamma_\Omega\rho](\Omega, t),$$
$$\text{with } \Gamma_\Omega P_0(\Omega) = 0 \quad (1)$$

$\mathcal{H}(\Omega)^X$ is the superoperator for the orientation-dependent spin Hamiltonian. Γ_Ω is a Markovian operator for the rotational reorientation of the spin-bearing moiety (probe), with the Euler angles $\Omega \rightarrow (\alpha, \beta, \gamma)$ (Ω_{CM} in the notation above) representing the orientational angles. $P_0(\Omega)$ represents the unique equilibrium probability distribution.

A simple form of the diffusion operator, Γ_Ω, is[21]

$$-\Gamma_\Omega = R\nabla_\Omega{}^2 P(\Omega, t) - (R/kT)(\sin\beta)^{-1}\partial/\partial\beta[\sin\beta \mathbf{T}P(\Omega, t)] \quad (2)$$

where R is the isotropic rotational diffusion rate, $\nabla_\Omega{}^2$ is the rotational diffusion operator in the Euler angles, Ω, and $\mathbf{T}$ is the restoring torque. The latter is equal to $\partial u/\partial\beta$ for an axial restoring potential, for example, $u \cong -3/2\ c_0^2(\cos\beta)^2$ (u is given in units of kT). The expression of Γ_Ω for rhombic diffusion tensor and rhombic potential is given in ref 22.

In this study, we are using an axial diffusion tensor, $\boldsymbol{R}$, yielding in the absence of any restricting potential three decay rates, $\tau_K^{-1} = 6R_\perp + K^2(R_\parallel - R_\perp)$, where $K = 0$, 1, and 2 (K is the order of the rank 2 diffusion tensor). $R_\parallel$ and $R_\perp$ are the principal values of $\boldsymbol{R}$; one may also define $\tau_\parallel = 1/(6R_\parallel)$ and $\tau_\perp = 1/(6R_\perp)$.[22]

For a uniaxial local director, one may expand the potential in the complete basis set of the Wigner rotation matrix elements with $M = 0$, $D^L_{0,K}(\Omega_{CM})$. One has[22]

$$u(\Omega_{CM}) = -\sum_{L=1}^{\infty}\sum_{K=-L}^{+L} c_K^L D^L_{0,K}(\Omega_{CM}) \quad (3)$$

with c_K^L being dimensionless. If only the lowest, $L = 2$, terms are preserved, one obtains the real potential[22]

DOI: 10.1021/acs.jpcb.8b06330
J. Phys. Chem. B 2018, 122, 8675−8684

$$u(\Omega_{CM}) \approx -c_0^2 D_{0,0}^2(\Omega_{CM}) - c_2^2[D_{0,2}^2(\Omega_{CM}) + D_{0,-2}^2(\Omega_{CM})] \quad (4)$$

with c_0^2 evaluating the strength of the potential, and c_2^2 its rhombicity.[24] This form of $u(\Omega_{CM})$ is used herein.

Local order parameters are defined as[22]

$$\langle D_{0,K}^2(\Omega_{CM})\rangle = \int d\Omega_{CM} D_{0,K}^2(\Omega_{CM}) \exp[-u(\Omega_{CM})] / \int d\Omega_{CM} \exp[-u(\Omega_{CM})] \qquad K = 0, 2 \quad (5)$$

For at least three-fold symmetry around the local director, C, and at least two-fold symmetry around the principal axis of the local ordering tensor, Z_M, only $S_0^2 \equiv \langle D_{0,0}^2(\Omega_{CM})\rangle$ and $S_2^2 \equiv \langle D_{0,2}^2(\Omega_{CM}) + D_{0,-2}^2(\Omega_{CM})\rangle$ survive.[22] The Saupe order parameters relate to irreducible tensor components, S_0^2 and S_2^2, as $S_{xx} = (3/2S_2^2 - S_0^2)/2$, $S_{yy} = -(3/2S_2^2 + S_0^2)/2$ and $S_{zz} = S_0^2$.

The ordering tensor, **S**, with principal values defined by eq 5, also has a specific orientation. To determine it, one includes in the analysis the transformation of its PAS, taken for convenience to be the same as the PAS of the local diffusion tensor, into the (known) PAS of the ^{2}H quadrupolar tensor. For rhombic potentials and a uniaxial local director the respective Wigner rotation features the Euler angles $\Omega_{MQ} = (\alpha_{MQ}, \beta_{MQ}, 0)$. With α_{MQ} set equal to zero (see above), the angle β_{MQ}, called "diffusion tilt", expresses the orientation of the ***S*** tensor with respect to the ***Q*** tensor.

3. RESULTS AND DISCUSSION

3.1. General Assessments.

(a) In all of the MOMD spectra shown below axially symmetric quadrupole interaction, with quadrupole constant Q = 180 kHz, is used.[24,25] An intrinsic linewidth, $(1/T_2)^*$, of 1 kHz is used; increasing it to 2 kHz has a small effect on the analysis.

(b) Let us estimate the strength of the local potential at the site of mobile phenyl rings in proteins. In simple cases, π-flips reproduce the experimental ^{2}H lineshapes.[47] They may be envisioned as 60° (or 120°) C−D jumps between equally populated ($p_1 = p_2$) exchanging sites, around the C^β−C^ξ axis (Figure 1).[48] In the extreme motional narrowing limit, one has $1/T_2 = \delta^2 \times (p_1 \times p_2)/k_{ex}$ ($1/T_2$. linewidth; δ, chemical-shift site separation; k_{ex}, jump/exchange rate). Diffusive motion yields in this limit $1/T_2 = \Delta^2 \times (S_0^2)^2 \times \tau$ for the simple potential, $u = -c_0^2 D_{00}^2$ (c_0^2, coefficient estimating potential strength; Δ, anisotropic magnetic interaction; $S_0^2 = \langle D_{00}^2\rangle$, axial order parameter; τ, correlation time for rotational diffusion); this is a simple MOMD limit. Thus, for very fast motion, $(S_0^2)^2$ in MOMD is formally analogous to $p_1 \times p_2$ in the π-flip mode. For $p_1 = p_2$, one has $p_1 \times p_2 = (S_0^2)^2 = 0.25$, which corresponds to $c_0^2 = 2.3$;[49] for $p_1 \neq p_2$, one has $(S_0^2)^2 < 0.25$, which corresponds to $c_0^2 < 2.3$. It is reasonable to assume that c_2^2 is comparable to c_0^2; within a preliminary approximation, both are thus expected to be on the order of 2 kT.

(c) The authors of ref 28 showed that jumps with angular separation of 60° (120°) around the C^β−C^ξ axis are equivalent to rotation with an angular separation of 64° (or 133°) around a tetrahedral axis. The latter geometric setup resembles to a greater degree rotational diffusion. We use this geometric perspective, drawing a formal analogy between the angle β_{MQ} in MOMD and the 64° angle.

3.2. Simulations. *3.2.1. Local Potential.* π-flips produce in the extreme motional narrowing limit a rhombic spectrum with three pairs of discontinuities located at $\pm Q_{xx} = \pm 3/8Q = \pm 67.55$ kHz; $\pm Q_{yy} = \pm 3/32Q = \pm 16.875$ kHz; and $\pm Q_{zz} = \pm 15/32Q = \pm 84.375$ kHz, yielding discontinuity-separations of 135, 33.75, and 168.75 kHz, respectively.[48] As shown below, all of the experimental spectra studied here exhibit pairs of discontinuities separated by ∼30 and ∼140 kHz. The proximity of these values to the motional narrowing values depicted above is an indication that $R_\parallel$ is relatively large and $R_\perp$ is relatively small (on the time-scale of the quadrupole interaction), with β_{MQ} being close to 64°.

On this basis, we vary log $R_\perp$ (log $R_\parallel$), keeping it relatively small (large), fix β_{MQ} at 64°, and use a potential strength of 2 kT as the preliminary benchmark. ^{2}H lineshapes calculated for c_0^2 in the 1.12−1.8 range and c_2^2 in the 1.73−2.6 range, with β_{MQ} = 64°, log $R_\perp$ = 2.5, and log $R_\parallel$ = 6.0, are shown in Figure 5. All of these spectra comprise inner discontinuities separated by approximately 30 kHz. Only the stronger potential with c_0^2 = 1.8 and c_2^2 = 2.6 also features outer discontinuities separated by approximately 140 kHz. This potential is taken as an improved benchmark.

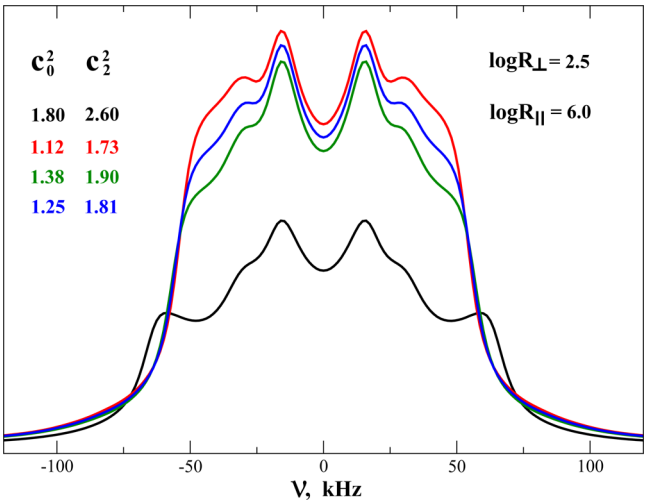

Figure 5. MOMD lineshapes calculated with log $R_\perp$ = 2.5, log $R_\parallel$ = 6.0, and the following potentials (eq 4): c_0^2 = 1.8 and c_2^2 = 2.6 (black); c_0^2 = 1.12 and c_2^2 = 1.73 (red); c_0^2 = 1.38 and c_2^2 = 1.9 (green); and c_0^2 = 1.25 and c_2^2 = 1.81 (blue). Additional parameters include Q = 180 kHz, β_{MQ} = 64° and an intrinsic linewidth of 1 kHz.

3.2.2. Local Motional Rates. We explore the effect of $R_\parallel$ and $R_\perp$, with β_{MQ} = 64, c_0^2 = 1.8 and c_2^2 = 2.6. Setting log $R_\perp$ = 2.5, as in Figure 5, we vary log $R_\parallel$ from 5.2 to 6.0 (Figure 6). The spectral shapes differ considerably for 5.2 < log $R_\parallel$ < 5.8, and rather moderately outside of this region. In the present setting, the log $R_\perp$ = 2.5 spectrum approaches the rigid limit, whereas the log $R_\parallel$ = 6.0 spectrum nears the fast-motion limit. The inner discontinuity separation of ∼30 kHz persists throughout. The outer discontinuity separation decreases, and the relative intensity of the inner-to-outer discontinuity increases, with increasing log $R_\parallel$.

In Figure 7, we fix log $R_\perp$ at 2.3 instead of 2.5, and vary log $R_\parallel$ in the 5.4−6.0 range, with all of the other parameters

DOI: 10.1021/acs.jpcb.8b06330
J. Phys. Chem. B 2018, 122, 8675−8684

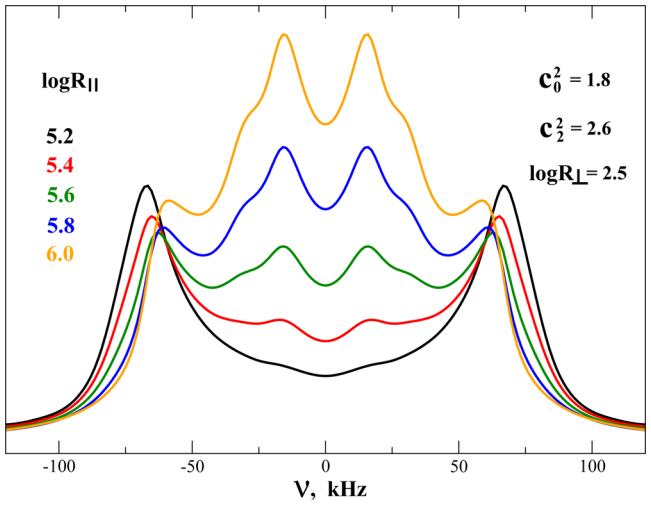

Figure 6. MOMD lineshapes calculated with $c_0^2 = 1.8$, $c_2^2 = 2.6$, log $R_\perp = 2.5$, and the following values of log $R_\parallel$: 5.2 (black), 5.4 (red), 5.6 (green), 5.8 (blue) and 6.0 (orange). Additional parameters as in the captions of Figure 5.

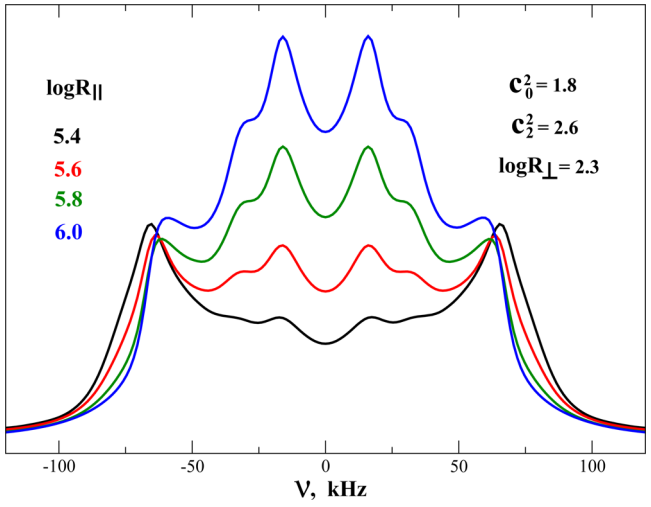

Figure 7. MOMD lineshapes calculated with $c_0^2 = 1.8$, $c_2^2 = 2.6$, log $R_\perp = 2.3$, and the following values of log $R_\parallel$: 5.4 (black), 5.6 (red), 5.8 (green) and 6.0 (blue). Additional parameters as in the captions of Figure 5.

the same as in Figure 6. The differences between corresponding spectra in Figures 4 and 5 are relatively small. To find out how much larger can $R_\perp$ be before substantially affecting the ^{2}H lineshape, we show in Figure 8 spectra obtained for log $R_\perp$ in the 2.3−2.8 range, log $R_\parallel = 6.0$, and the parameters c_0^2, c_2^2, and β_{MQ} as in Figure 6. For log $R_\perp < 2.8$, the main effect consists of decrease in the visible part of the spectral plot with increasing log $R_\parallel$. For log $R_\perp = 2.8$, the shape of the spectrum also changes; larger values are expected to have a noticeable effect on the ^{2}H lineshape.

The effect of log $R_\parallel$ exceeding 6.0 on the ^{2}H spectrum consists primarily of an increase in the visible part of the spectral plot. Note that the resonances contributing to dynamic powder spectra from deuterated phenyl rings extend over the extensive range of $\pm 3/2Q = \pm 135$ kHz. Within the $\pm 3/4Q$ kHz region, the resonance intensity is relatively large; outside of this region, it is relatively small, often so small as not to contribute visibly to the spectral plot that shows the main

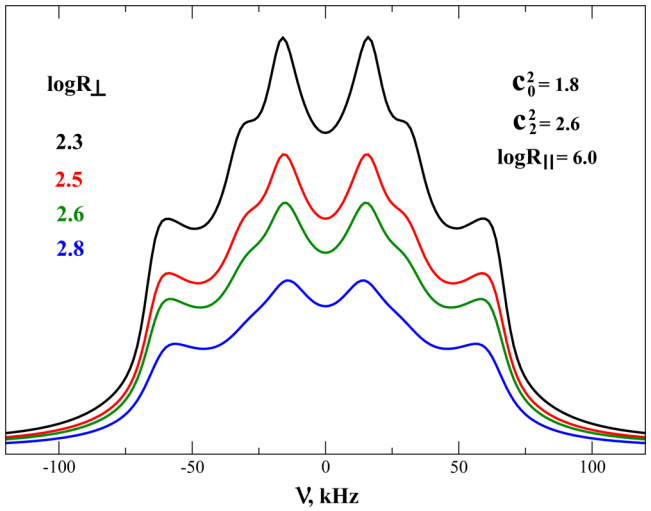

Figure 8. MOMD lineshapes calculated with $c_0^2 = 1.8$, $c_2^2 = 2.6$, log $R_\parallel$ = 6.0, and the following values of log $R_\perp$: 2.3 (black), 2.5 (red), 2.6 (green) and 2.8 (blue). Additional parameters as in the captions of Figure 5.

contributions. The part visible in a given spectrum depends on its shape, determined by the MOMD parameters c_0^2, c_2^2, R, and β_{MQ}.

3.2.3. Diffusion Tilt. Figure 9 illustrates the effect of lowering the value of β_{MQ} from 64° to 63°. Three pairs of ^{2}H

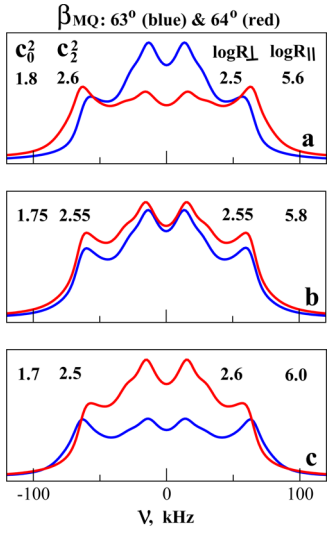

Figure 9. MOMD lineshapes calculated with the following parameter-sets: $c_0^2 = 1.8$, $c_2^2 = 2.6$, log $R_\perp = 2.5$ and log $R_\parallel = 5.6$ (part a); $c_0^2 = 1.75$, $c_2^2 = 2.55$, log $R_\perp = 2.55$ and log $R_\parallel = 5.8$ (part b); and $c_0^2 = 1.7$, $c_2^2 = 2.5$, log $R_\perp = 2.6$ and log $R_\parallel = 6.0$ (part c). Additional parameters as in the captions of Figure 5.

lineshapes, with c_0^2 (c_2^2) in the vicinity of 1.8 (2.6), log $R_\perp$ in the 2.5−2.6 range, and log $R_\parallel$ in the 5.6−6.0 range, are shown. The constituents of the pairs displayed in Figure 9a,c differ considerably; the respective changes feature opposite trends. The constituents of the pair displayed in Figure 9b differ to a small extent. The inner discontinuity separation is smaller for 63° as compared to 64°. Thus, the "local geometry" is an influential factor; not allowing β_{MQ} to vary is a significant simplification of the analysis, which we consider appropriate in view of the data-related limitations. However, Figures 5−8

DOI: 10.1021/acs.jpcb.8b06330
J. Phys. Chem. B 2018, 122, 8675−8684

indicate that even with β_{MQ} fixed at 64°, $R_{\parallel}$ near the fast-motion limit and $R_{\perp}$ near the rigid limit, the MOMD model is likely to be useful in analyzing the experimental phenyl-ring data.

3.3. Data Fitting. *3.3.1. Aβ_{40} Fibrils.* Figures 10a, 11a, and 12a show the experimental ^{2}H lineshapes yielded by the dry 3-fold symmetric twisted Aβ_{40} fibrils (3fd), the hydrated 3-fold symmetric twisted Aβ_{40} fibrils (3fw), and the hydrated protofibrils of the D23N mutant, respectively.[25] For each sample, there are three spectra acquired at 278 (black), 295 (blue), and 308 (red) K.

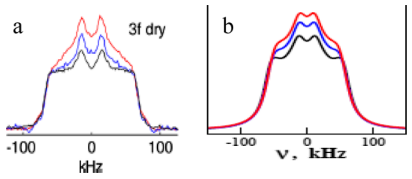

Figure 10. Experimental quadrupole echo ^{2}H spectra from the ^{2}H-labeled phenyl ring of F19 in the dry 3-fold-symmetric Aβ_{40}-amyloid fibril (3fd) (part a). Best-fit MOMD spectra calculated with the parameters depicted in Table 1. Q = 180 kHz, β_{MQ} = 64° and the intrinsic linewidth is 1 kHz (part b).

The three 278 K lineshapes differ mainly in the outer shoulders, and the region connecting the inner and outer discontinuities being slanted to different degrees. The three 295 K spectra (blue), and the three 308 K spectra (red), differ to a limited extent. The central HDO peak might not affect the various lineshapes in the same way.

We start with the ^{2}H lineshapes of 3fd, where HDO is absent. The experimental spectra are shown in Figure 10a.[25] An extended search with c_0^2 and c_2^2 varied in the 1.4−2.8 range, and log $R_{\perp}$ (log $R_{\parallel}$) in the 2.3−3.4 (5.6−6.4) range, led to the best-fit MOMD spectra shown in Figure 10b. In general, the latter reproduces the main features of the experimental spectra shown in Figure 10a. The widths of the inner discontinuities are overestimated. The agreement could be improved by allowing the intrinsic linewidth to be orientation-dependent. The commonly used expression[16] is $(1/T_2(\beta_{LC}))^* = (1/T_2)^* + \cos^2\beta_{LC} \times (1/T_2)^*$ [where β_{LC} is defined by $\Omega(0, \beta_{LC}, 0)$—cf. Figure 1]. The trend is appropriate, as $(1/T_2(\beta_{LC}))^*$ is narrower for larger β_{LC} (in the $0-\pi/2$ range) that is, for smaller discontinuity separation. Within the scope of the rationale underlying the present analysis, we account for this feature qualitatively. Similar considerations apply to Figure 11.

The best-fit parameters associated with Figure 10b are given in Table 1. The strength of the potential is 1.7 kT at 278 and 295 K, and slightly weaker at 308 K. The rhombicity of the potential is 2.6 kT at 278 and 295 K, and slightly smaller at 308 K. The order parameters, S_0^2 and S_2^2, were calculated from c_0^2 and c_2^2 according to eq 5. S_2^2 is close to 0.5, in evidence of "perpendicular ordering". Indeed, according to Figure 1, the main MOMD ordering axis is likely to orient preferentially perpendicular to the local director, defined as the average orientation of the C−D bond. log $R_{\perp}$ (log $R_{\parallel}$) increases from 3.0 to 3.3 (6.0 to 6.3) upon increasing the temperature from 278 to 308 K. Estimated activation energies are (16.6 ± 0.8) kJ/mol for $R_{\parallel}$ and (22.3 ± 1.1) kJ/mol for $R_{\perp}$. These values are within the (wide) range of activation energies determined for phenyl-ring dynamics in different systems.[24,25,28−33,47]

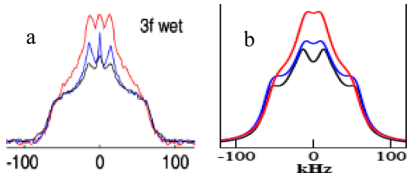

Figure 11. Experimental quadrupole echo ^{2}H spectra from the ^{2}H-labeled phenyl ring of F19 in the hydrated 3-fold-symmetric Aβ_{40}-amyloid fibril (3fw) (part a). Best-fit MOMD spectra calculated with the parameters depicted in Table 2. Additional parameters as in the captions of Figure 10b (part b).

Table 1. Best-Fit Values of c_0^2, c_2^2, log $R_{\perp}$, and log $R_{\parallel}$ Associated with the Best-Fit MOMD Spectra of Figure 10b, Which Reproduce the Experimental Spectra of the Dry 3-Fold Symmetric Aβ_{40} Fibrils (3fd) Shown in Figure 10a[a]

	c_0^2	c_2^2	S_0^2	S_2^2	log $R_{\perp}$	log $R_{\parallel}$
278 K	1.7	2.6	0.088	0.545	3.0	6.0
295 K	1.7	2.6	0.088	0.545	3.2	6.2
308 K	1.6	2.5	0.082	0.541	3.3	6.3

[a]Best-fit order parameters, S_0^2 and S_2^2, calculated according to eq 5. The average error is ±0.03 in c_0^2, c_2^2, log $R_{\perp}$, and log $R_{\parallel}$.

Figure 11a shows the experimental spectra of the 3fw fibril variant.[25] The best-fit MOMD spectra are shown in Figure 11b. The agreement between calculated and experimental spectra is good at 278 and 308 K and not so good at 295 K. However, in the 295 K spectrum, the inner discontinuities and the HDO peak are narrower than their counterparts at both lower and higher (on average, by 15°) temperatures. This behavior is difficult to reconcile; it might arise from experimental imperfection, or an unknown effect operating at 295 K, not accounted for in the current MOMD calculations.

The best-fit parameters associated with Figure 11b are given in Table 2. To determine the effect of hydration, we compare the data shown in Tables 1 and 2. The potential strength is the same at 278 and 295 K, and slightly weaker at 308 K in the hydrated sample. The rhombicity of the potential is similar in magnitude, with slightly different trends as a function of temperature in the dry and hydrated samples. In Table 2, the rhombicity increases with the increasing temperature. Similar behavior was observed for methyl moiety dynamics in globular proteins[17] and Aβ-amyloid fibrils,[20] and interpreted in terms of degrees of freedom that contribute to the rhombicity of the potential at higher temperatures being "frozen" at lower temperatures. We suggest that interpretation in the present case. The motional rates are the same in Tables 1 and 2 except for the 278 K spectra, where hydration renders diffusion more axially symmetric through reduction in the value of $R_{\perp}$.

Table 2. Best-Fit Values of c_0^2, c_2^2, log $R_{\perp}$, and log $R_{\parallel}$ Associated with the Best-Fit MOMD Spectra of Figure 11b, Which Reproduce the Experimental Spectra of the Hydrated 3-Fold Symmetric Aβ_{40} Fibrils (3fw) Shown in Figure 11a[a]

	c_0^2	c_2^2	S_0^2	S_2^2	log $R_{\perp}$	log $R_{\parallel}$
278 K	1.7	2.4	0.123	0.503	2.9	6.0
295 K	1.7	2.6	0.088	0.545	3.2	6.2
308 K	1.7	2.4	0.123	0.503	3.3	6.3

[a]Best-fit order parameters, S_0^2 and S_2^2. Average errors as in the title of Table 1.

DOI: 10.1021/acs.jpcb.8b06330
J. Phys. Chem. B 2018, 122, 8675−8684

Figure 12a shows the experimental spectra of the hydrated D23N protofibrils.[25] The best-fit spectra are shown in Figure 12b. The latter reproduce the main features of the experimental spectra shown in Figure 12a. The purpose of the augmented line thickness is to include the error in the graphical illustration.

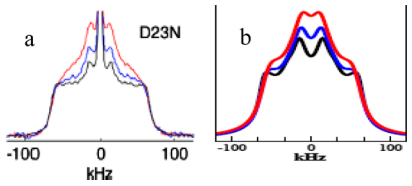

Figure 12. Experimental quadrupole echo ^{2}H spectra from the ^{2}H-labeled phenyl ring of F19 in the hydrated protofibrils of the D23N mutant of Aβ_{40}-amyloid peptide (part a). Best-fit MOMD spectra calculated with the parameters depicted in Table 3. Additional parameters as in the captions of Figure 10b (part b).

The best-fit parameters associated with Figure 12b are given in Table 3. The potential strength is constant, with $c_0^2 = 1.7$.

Table 3. Best-Fit Values of c_0^2, c_2^2, log $R_\perp$, and log $R_\parallel$ Associated with the Best-Fit MOMD Spectra of Figure 12b, Which Reproduce the Experimental Spectra of the Hydrated D23N Protofibrils Depicted in Figure 12a[a]

	c_0^2	c_2^2	S_0^2	S_2^2	log $R_\perp$	log $R_\parallel$
278 K	1.7	2.4	0.123	0.503	2.7	5.9
295 K	1.7	2.6	0.088	0.545	3.0	6.0
308 K	1.7	2.5	0.106	0.524	3.2	6.2

[a]Best-fit order parameters, S_0^2 and S_2^2. Average errors as in the title of Table 1.

The rhombicity of the potential (c_2^2) is 2.4, 2.6, and 2.5 at 278, 295, and 308 K, respectively. log $R_\perp$ increases from 2.7 to 3.2 and log $R_\parallel$ from 5.9 to 6.2, upon increasing the temperature from 278 to 308 K. Estimated activation energies are (27.4 ± 1.4) kJ/mol for $R_\parallel$ and (19.1 ± 1.0) kJ/mol for $R_\perp$.

In general, the strength of the potential and its rhombicity do not differ much from those of the WT fibrils. On the other hand, both $R_\perp$ and $R_\parallel$ are substantially smaller for the D23N protofibrils as compared to the WT fibrils. This is an interesting feature. Further studies are required to determine its source, which could be differences in the secondary structure and/or monomer assembly and/or antiparallel versus parallel β-sheet architecture.

Finally, we compare phenyl-ring dynamics in the hydrated 3-fold symmetric twisted WT fibrils (3fw, Figure 11a) and the hydrated 2-fold-symmetric striated-ribbon fibrils[25] (2fw, Figure S1 of the Supporting Information). The 295 and 308 K spectra are quite similar; the 278 K spectra differ, with the 2fw spectrum exhibiting increased depression in the region connecting the outer and inner divergences, and steeper rise from the baseline of the outer divergences.

Figure 13a illustrates the parameter variations that bring about such spectral changes: larger c_0^2, no change in c_2^2, smaller log $R_\perp$, and smaller log $R_\parallel$. Within the scope of methyl-moiety dynamics, virtually no difference was observed experimentally between 2fw and 3fw in the region of the peptide structure housing the F19 sidechain.[20]

MOMD Versus MSM. MOMD describes "restricted phenyl-ring dynamics" expressing the "restrictions" by a physically well-defined rhombic potential and the "dynamics" by an axial second-rank diffusion tensor. This model reproduces the main features of the experimental ^{2}H lineshapes; it yields a consistent and physically relevant picture.

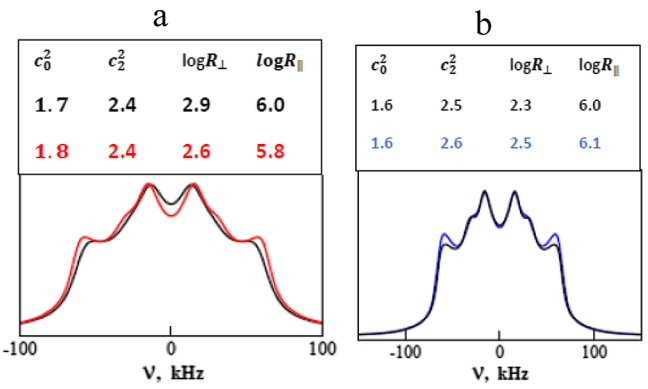

Figure 13. MOMD lineshapes calculated with $c_0^2 = 1.7$, $c_2^2 = 2.4$, log $R_\perp = 2.9$ and log $R_\parallel = 6.0$, referring to 3fw (black); and $c_0^2 = 1.8$, $c_2^2 = 2.4$, log $R_\perp = 2.6$ and log $R_\parallel = 5.8$, referring to 2fw (red) (part a). MOMD lineshapes calculated with $c_0^2 = 1.6$, $c_2^2 = 2.5$, log $R_\parallel = 2.3$ and log $R_\parallel = 6.0$, referring to F58 in hydrated HP36 (black); $c_0^2 = 1.6$, $c_2^2 = 2{,}6$, log $R_\perp = 2.5$ and log $R_\parallel = 6.1$, referring to F58 in dry HP36 (blue) (part b). Additional parameters as in the captions of Figure 10b.

The MSM model for phenyl-ring dynamics in the Aβ_{40}-amyloid fibrils is depicted schematically in the upper part of Figure 14A.[25] It features two different motions involving the dihedral angle χ_2. Assuming strong collision, these motions are large-angle flips between sites 1−3 and 2−4, and small-angle fluctuations between sites 1−2 and 3−4, independent of one another. The rates of these motions, k^{large} and k^{small}, are assumed to exhibit Arrhenius-type temperature dependence. The respective activation energies are assumed to be distributed around mean values, E_a^{large} and E_a^{small}. The parameter E_a^{large} (E_a^{small}) is associated with Gaussian (Gamma) distribution with width σ^{large} (σ^{small}). E_a^{large} and E_a^{small} are taken to be independent of temperature. The parameters allowed to vary in the data-fitting process are E_a^{large}, E_a^{small}, σ^{large}, σ^{small}, and the two pre-exponential factors in the Arrhenius equation, with the latter four parameters allowed to vary with temperature.

The local potential is parameterized after data fitting in terms of E_a^{large} and E_a^{small} (Figure 14B). Note that the local potential and the activation energy for local motion are related, but not the same, physical quantities. On the basis of the pre-exponential factors and the activation energies given in ref 25, we calculated log(k^{large}) (log(k^{small})) to be in the 5.5−7.0 (8.2−8.6) range. It is difficult to envision large-angle flips occurring between the sites 1−3 and 2−4, while the sites 1−2 and 3−4 are averaged at a much faster rate.

3.3.2. HP36 Protein. Only a single ^{2}H spectrum acquired at 295 K is available for the phenyl rings of F51 and F58 in the hydrated protein;[24] they do not differ much. For F58, the 295 K ^{2}H spectrum of the dry protein is also available. Figure S2 of the Supporting Information shows the hydrated (black) and dry (blue) spectra of F58 superposed.[24] They differ by enhanced concavity of the region connecting the inner and outer divergences and slightly larger inner-to-outer-divergence intensity ratio in the spectrum of the hydrated sample. Figure 13b shows parameter variations that can bring about such spectral changes. It points to less rhombic potential (smaller c_2^2) and more axial local diffusion (larger $R_\parallel/R_\perp$, in particular due to smaller $R_\perp$) in the hydrated sample.

DOI: 10.1021/acs.jpcb.8b06330
J. Phys. Chem. B 2018, 122, 8675−8684

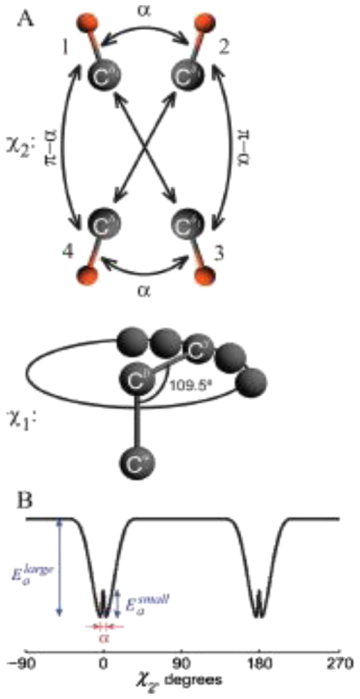

Figure 14. MSM model used to analyze phenyl dynamics in the fibril variants [upper part of (A), and (B)]. Large-angle ring-flips occur between sites 1 and 3, as well as 2 and 4, with rate k^{large}. Small-angle fluctuations occur between sites 1 and 2, as well as 3 and 4, with rate k^{small}. The activation energies for k^{large} (k^{small}) exhibit Gaussian (Gamma) distribution with mean E_a^{large} (E_a^{small}) and width σ^{large} (σ^{small}). E_a^{large} and E_a^{small}, depicted in (B), are considered to represent the local potential. The MSM model for phenyl dynamics in HP36 comprises in addition the motion illustrated in the lower part of (A)—nearest-neighbor jumps occurring with rate k along an arc of length l centered at the $C^{\alpha}-C^{\beta}$ bond.[25]

Table 4 shows the MOMD parameters corresponding to the 295 K spectrum of F58 in hydrated HP36 (row 1); the 295 K spectrum of F19 in 3fw (row 2); and the 295 K spectrum of F19 in hydrated D23N (row 3). All of the parameters associated with HP36 differ from the corresponding parameters associated with the Aβ_{40} fibrils. The largest discrepancy is associated with log $R_{\perp}$, which is 2.3 in HP36 and 3.2 (3.0) in 3fw (hydrated D23N). The difference between the globular protein HP36 and the Aβ_{40}-amyloid fibrils is substantial in the present context.

Table 4. c_0^2, c_2^2, log $R_{\perp}$, and log $R_{\parallel}$ Corresponding to the 295 K Spectrum of F58 in Hydrated HP36 (Row 1); the 295 K Spectrum of F19 in 3fw (Row 2); and the 295 K Spectrum of F19 in Hydrated D23N (Row 3)[a]

row no.	probe	c_0^2	c_2^2	S_0^2	S_2^2	log $R_{\perp}$	log $R_{\parallel}$
1	F58 in HP36	1.6	2.5	0.082	0.541	2.3	6.0
2	F19 in 3fw	1.7	2.6	0.088	0.545	3.2	6.2
3	F19 in D23N	1.7	2.6	0.088	0.545	3.0	6.0

[a]Order parameters, S_0^2 and S_2^2.

To reproduce the enhanced concavity of the region connecting the inner and outer divergences with MSM, an additional mode—small nearest-neighbor jumps along an arc centered at the $C^{\alpha}-C^{\beta}$ bond—was included in the overall model.[24]

3.4. New Insights Based on MOMD. The structural dynamics of all of the phenyl rings studied here have been interpreted in terms of two physical quantities—the local potential, u, and the local diffusion tensor, $\boldsymbol{R}$. This made possible comparing phenyl-ring sites of dry and hydrated fibrils, Aβ_{40} fibrils and protofibrils of the D23N-mutant, 2-fold-, and 3-fold-symmetric Aβ_{40} fibrils, and dry and hydrated HP36 (see above). Importantly, the globular and fibril-type protein forms have been compared.

Let us relate these results to the HP36 structure (Figure 2) and the monomer structures of the various fibril variants studied (Figure 3). Protein hydration affects the phenyl rings of F51 and F58 (ref 25 and this study) of HP36. It also affects the methyl groups of L75, L61, and V50, but not the methyl groups of L69.[13,17] All of these structural elements are depicted in Figure 2. The L69 methyl groups are located adjacent to, and eventually pack against, the protein scaffold. All of the other side chains appear to be associated with enough "free volume" to let water penetrate and affect their motion.

The MSM for methyl-moiety dynamics[13] differs from the MSM for phenyl-ring dynamics;[25] hence, comparison between the two probe types cannot be conducted. MOMD analyzes all the probes with the same model. It points to u and $R_{\perp}$ being similar for phenyl rings and methyl groups, $R_{\parallel}$ being faster for phenyl rings, and the local geometry being more intricate for methyl moieties (ref 20 and this study).

Let us focus on the Aβ_{40} fibril variants. Among the methyl groups of L17, L34, M35, and V36 (with M35 depicted in Figure 3a–c and L34 depicted in Figure 3a,b), only the M35 methyl is affected by fibril hydration.[13,20] We have shown[20] that hydration-related aspects are propagated selectively through the interaction of the M35 methyl with tightly peptide-bound water.[20] Independently, it was shown that the M35 methyl exhibits intermonomer orientation.[50] We find here that the F19 phenyl ring is also affected by fibril hydration. Inspection of Figure 3—in particular, Figure 3c, see phenyl ring of F19 located between V18 and F20—shows that the F19 side chain is pointing away from the monomer plane. This is a position where (similar to the M35 methyl) the F19 phenyl ring could interact with tightly peptide-bound water, explaining its detected response to fibril hydration.

Finally, as outlined above in detail, phenyl-ring dynamics in the Aβ_{40} fibrils differ considerably from phenyl-ring dynamics in HP36.

The following comments with regard to the MOMD analysis are of interest. (1) The local potential is defined here in terms of the coefficients c_0^2 and c_2^2 of the potential $u(\Omega_{CM})$ (eq 4). One may also represent $u(\Omega_{CM})$, and the associated probability distribution $\exp(-u(\Omega_{CM}))$, as 3D pictures (or 2D projections thereof). Such pictures are shown in ref 17 (Figure 7) and ref 51 (Figures 7–9). For illustration, we show in Figure S3 of the Supporting Information the 3D plot and associated probability distribution for the potentials with c_0^2 = 1.8, c_2^2 = 2.6, and c_0^2 = 1.2, c_2^2 = 1.8, used (among others) in Figure 5. (2) One could improve the agreement with the experiment by allowing additional MOMD parameters to vary in the data-fitting process. However, different cases would require different additional variables. This would impair consistency, which we set as (justified) objective within the scope of capturing key features of limited experimental data sets. (3) The calculated MOMD spectra exhibit quite a few features not observed in continuous wave (CW) experimental spectra, such as treated in this study. Recently, we developed MOMD for the analysis

DOI: 10.1021/acs.jpcb.8b06330
J. Phys. Chem. B 2018, 122, 8675–8684

of ^{2}H spectra acquired in the presence of magic angle spinning (MAS).[19] Such spectra are better resolved than CW spectra (ref 19 and articles cited therein). Applications of MOMD/MAS are expected to bear out the benefits of enhanced resolution.

4. CONCLUSIONS

The MOMD approach as applied to ^{2}H lineshape analysis in the solid state was used to study restricted phenyl-ring dynamics in several Aβ_{40}-amyloid-fibril variants and the villin headpiece subdomain HP36. The available experimental data are limited in extent and sensitivity. Out of the three key quantities characterizing restricted motions—local potential, u, local diffusion tensor, $\boldsymbol{R}$, and local geometry—the former two were allowed to vary in analyzing the ^{2}H lineshapes, while the local geometry was fixed according to standard stereochemistry. With this strategy, the main features of the experimental lineshapes were reproduced, and a consistent physically relevant picture of phenyl-ring dynamics was obtained. In the 278−308 K temperature range, the strength of u is (1.7−1.8) kT and its rhombicity is (2.4−2.6) kT; the rate constants for local motion are $5.0 \times 10^2 \leq R_\perp \leq 2.0 \times 10^3$ s^{-1} and $6.3 \times 10^5 \leq R_\parallel \leq 2.0 \times 10^6$ s^{-1}.

At 278 K, phenyl-ring diffusion in the 3fw polymorph is more symmetric than in the 2fw polymorph, mainly because of smaller $R_\perp$. F19 phenyl-ring motion is slower in the D23N protofibril than in the WT fibrils. Hydrated HP36 exhibits more symmetric phenyl-ring potentials and diffusion tensors than dry HP36. At 295 K, the local potential and the local diffusion associated with the HP36 phenyl rings differ from their counterparts associated with the fibril phenyl rings.

The M35 methyl and the F19 phenyl ring are affected by the hydration of their host fibril. This is due to intermonomer orientation, which facilitates interactions with tightly peptide-bound water, shown in previous work to propagate hydration-related aspects.[20]

The phenyl rings of F51 and F58, and the methyl-moieties of V50, L61, and L75, all of which reside in the HP36 core, benefit from sufficient free space to allow for water access; hence, they respond to protein hydration.

From the perspective of phenyl-ring dynamics, the Aβ_{40} fibrils and HP36 differ considerably. The ^{2}H phenyl-ring spectra considered here were analyzed previously with MSM models; the latter aimed at precise reproduction of the experimental ^{2}H lineshapes. For that, two (for the Aβ_{40} fibrils) and three (for HP36) simple dynamic modes were combined, and quite a few assumptions were made. Phenyl-ring dynamics is described in terms of distributions in temperature-independent mean activation energies. This interpretation differs fundamentally from the MOMD-based interpretation.

Finally, the pervasive problem of experimental data limited in extent and sensitivity is being addressed here effectively.

■ ASSOCIATED CONTENT

Supporting Information

The Supporting Information is available free of charge on the ACS Publications website at DOI: 10.1021/acs.jpcb.8b06330.

^{2}H quadrupole-echo spectra of F19 in the hydrated 2-fold symmetric striated-ribbon Aβ_{40} amyloid fibril variant at 278, 295 and 308 K (Figure S1); ^{2}H quadrupole-echo spectra of F58 at 295 K in hydrated and dry HP36 (Figure S2): 3D plots of the potentials $u = -1.8D^2_{0,0} - 2.6(D^2_{0,2} + D^2_{0,-2})$ and $u = -1.2D^2_{0,0} - 1.8(D^2_{0,2} + D^2_{0,-2})$, as well as the associated probability distributions, $\exp(-u)$ (PDF)

■ AUTHOR INFORMATION

Corresponding Author

*E-mail: eva.meirovitch@biu.ac.il. Phone: 972-3-531-8049 (E.M.).

ORCID

Eva Meirovitch: 0000-0001-5117-5079

Jack H. Freed: 0000-0003-4288-2585

Notes

The authors declare no competing financial interest.

■ ACKNOWLEDGMENTS

This work was supported by the Israel—U.S.A. Binational Science Foundation (grant no. 2016097 to E.M. and J.H.F.) and the Israel Science Foundation (grant no. 469/15 to E.M.). This work was also supported by NIH/NIGMS grant P41GM103521 to J.H.F.

■ REFERENCES

(1) Spiess, H. W. *Dynamic NMR Spectroscopy*; Diehl, P., Fluck, E., Kosfeld, R., Eds.; Springer Verlag, 1978; Vol. *15*, pp 55−241.

(2) Huang, T. H.; Skarjune, R. P.; Wittebort, R. J.; Griffin, R. G.; Oldfield, E. Restricted Rotational Isomerization in Polymethylene Chains. *J. Am. Chem. Soc.* **1980**, *102*, 7377−7379.

(3) Batchelder, L. S.; Sullivan, C. E.; Jelinski, L. W.; Torchia, D. A. Characterization of leucine side-chain reorientation in collagen-fibrils by solid-state 2H NMR. *Proc. Natl. Acad. Sci. U.S.A.* **1982**, *79*, 386−389.

(4) Vold, R. R.; Vold, R. L. Deuterium Relaxation in Molecular Solids. *Adv. Magn. Opt. Reson.* **1991**, *16*, 85−171.

(5) Alam, T. M.; Drobny, G. P. Solid-State NMR Studies of DNA Structure and Dynamics. *Chem. Rev.* **1991**, *91*, 1545−1590.

(6) *Solid-State NMR Studies of Biopolymers*; McDermott, A. E., Polenova, T., Eds.; John Wiley and Sons: U.K., 2010.

(7) Krushelnitsky, A.; Reichert, D.; Saalwächter, K. Solid-State NMR Approaches to Internal Dynamics of Proteins: from Picoseconds to Microseconds and Seconds. *Acc. Chem. Res.* **2013**, *46*, 2028−2036.

(8) Lewandowski, J. R. Advances in Solid-State Relaxation Methodology for Probing Site-Specific Protein Dynamics. *Acc. Chem. Res.* **2013**, *46*, 2018−2027.

(9) Watt, E. D.; Rienstra, C. M. Recent Advances in Solid-State Nuclear Magnetic Resonance Techniques to Quantify Biomolecular Dynamics. *Anal. Chem.* **2013**, *86*, 58−64.

(10) Schanda, P.; Ernst, M. Studying dynamics by magic-angle spinning solid-state NMR spectroscopy: Principles and applications to biomolecules. *Prog. Nucl. Magn. Reson. Spectrosc.* **2016**, *96*, 1−46.

(11) Vold, R. L.; Hoatson, G. L. Effects of Jump Dynamics on Solid State Nuclear Magnetic Resonance Line Shapes and Spin Relaxation Times. *J. Magn. Reson.* **2009**, *198*, 57−72.

(12) Echodu, D.; Goobes, G.; Shajani, Z.; Pederson, K.; Meints, G.; Varani, G.; Drobny, G. Furanose Dynamics in theHhaI Methyltransferase Target DNA Studied by Solution and Solid-State NMR Relaxation. *J. Phys. Chem. B* **2008**, *112*, 13934−13944.

(13) Vugmeyster, L.; Ostrovsky, D. Static solid-state 2 H NMR methods in studies of protein side-chain dynamics. *Prog. Nucl. Magn. Reson. Spectrosc.* **2017**, *101*, 1−17.

(14) Mason, R. P.; Polnaszek, C. F.; Freed, J. H. Interpretation of electron spin resonance spectra of spin labels undergoing very anisotropic rotational reorientation. Comments. *J. Phys. Chem.* **1974**, *78*, 1324−1329.

(15) Meirovitch, E.; Freed, J. H. Slow motional NMR lineshapes for very anisotropic diffusion: I = 1 nuclei. *Chem. Phys. Lett.* **1979**, *64*, 311−316.

DOI: 10.1021/acs.jpcb.8b06330
J. Phys. Chem. B 2018, 122, 8675−8684

(16) Meirovitch, E.; Nayeem, A.; Freed, J. H. Analysis of protein-lipid interactions based on model simulations of electron spin resonance spectra. *J. Phys. Chem.* **1984**, *88*, 3454−3465.
(17) Meirovitch, E.; Liang, Z.; Freed, J. H. Protein Dynamics in the Solid State from 2H NMR Line Shape Analysis: A Consistent Perspective. *J. Phys. Chem. B* **2015**, *119*, 2857−2868.
(18) Meirovitch, E.; Liang, Z.; Freed, J. H. Protein Dynamics in the Solid State from 2H NMR Line Shape Analysis. II. MOMD Applied to C-D and C-CD3 Probes. *J. Phys. Chem. B* **2015**, *119*, 14022−14032.
(19) Meirovitch, E.; Liang, Z.; Freed, J. H. Protein dynamics in the solid-state from 2 H NMR lineshape analysis. III. MOMD in the presence of Magic Angle Spinning. *Solid State Nucl. Magn. Reson.* **2018**, *89*, 35−44.
(20) Meirovitch, E.; Liang, Z.; Freed, J. H. MOMD Analysis of NMR Lineshapes from Aβ-Amyloid Fibrils: A New Tool for Characterizing Molecular Environments in Protein Aggregates. *J. Phys. Chem. B* **2018**, *18*, 4793−4801.
(21) Polnaszek, C. F.; Bruno, G. V.; Freed, J. H. ESR line shapes in the slow-motional region: Anisotropic liquids. *J. Chem. Phys.* **1973**, *58*, 3185−3199.
(22) Polnaszek, C. F.; Freed, J. H. Electron Spin Resonance Studies of Anisotropic Ordering, Spin Relaxation, and Slow Tumbling in Liquid Crystalline Solvents. *J. Phys. Chem.* **1975**, *79*, 2283−2306.
(23) Polimeno, A.; Freed, J. H. Slow Motional ESR in Complex Fluids: The Slowly Relaxing Local Structure Model of Solvent Cage Effects. *J. Phys. Chem.* **1995**, *99*, 10995−11006.
(24) Vugmeyster, L.; Ostrovsky, D.; Villafranca, T.; Sharp, J.; Xu, W.; Lipton, A. S.; Hoatson, G. L.; Vold, R. L. Dynamics of Hydrophobic Core Phenylalanine Residues Probed by Solid-State Deuteron NMR. *J. Phys. Chem. B* **2015**, *119*, 14892−14904.
(25) Vugmeyster, L.; Clark, M. A.; Falconer, I. B.; Ostrovsky, D.; Gantz, D.; Qiang, W.; Hoatson, G. L. Flexibility and Solvation of Amyloid-β Hydrophobic Core. *J. Biol. Chem.* **2016**, *291*, 18484−18495.
(26) Wüthrich, K.; Wagner, G. NMR investigations of the dynamics of the aromatic amino acid residues in the basic pancreatic trypsin inhibitor. *FEBS Lett.* **1975**, *50*, 265−268.
(27) Kasinath, V.; Fu, Y.; Sharp, K. A.; Wand, A. J. A Sharp Thermal Transition of Fast Aromatic-Ring Dynamics in Ubiquitin. *Angew. Chem., Int. Ed. Engl.* **2015**, *54*, 102−107.
(28) Shadt, R. J.; Cain, E. J.; English, A. D. Simulation of One-Dimensional ^{2}H NMR Line Shapes. *J. Phys. Chem.* **1993**, *97*, 8387−8392.
(29) Zhang, H.; Bryant, R. G. Characterization of Enzyme-Bound Ligand Dynamics by Solid-State NMR in the Presence of Ligand Exchange: L-Phenylalanine on Carboxypeptidase A. *Biophys. J.* **1995**, *68*, 303−311.
(30) Hiroaki, T.; Kogame, A.; Nishi, N.; Tsutsumi, A. Deuterium NMR Studies on Phenyl Ring Dynamics of Poly(L-phenylalanine). *J. Mol. Struct.* **1998**, *441*, 243−250.
(31) Naito, A.; Iizuka, T.; Tuzi, S.; Price, W. S.; Hayamizu, K.; Saitô, H. Phenyl ring dynamics of the insulin fragment Gly-Phe-Phe(B23-B25) by solid state deuterium NMR. *J. Mol. Struct.* **1995**, *355*, 55−60.
(32) Hirschinger, J.; Miura, H.; Gardner, K. H.; English, A. D. Segmental dynamics in the crystalline phase of nylon 66: solid state deuterium NMR. *Macromolecules* **1990**, *23*, 2153−2169.
(33) Burke, P. A.; Griffin, R. G.; Klibanov, A. M. Solid-State nuclear magnetic resonance investigation of solvent dependence of tyrosyl ring motion in an enzyme. *Biotechnol. Bioeng.* **1993**, *42*, 87−94.
(34) Meirovitch, E.; Shapiro, Y. E.; Zerbetto, M.; Polimeno, A. SRLS Analysis of 15N Spin Relaxation from E. coli Ribonuclease HI: The Tensorial Perspective. *J. Phys. Chem. B* **2012**, *116*, 886−894.
(35) Bretscher, A.; Weber, K. Villin is a major protein of the microvillus cystoskeleton which binds both G and F actin in a calcium-dependent manner. *Cell* **1980**, *20*, 839−847.
(36) McKnight, J. C.; Doering, D. S.; Matsudaira, P. T.; Kim, P. S. A Thermostable 35-Residue Subdomain within Villin Headpiece. *J. Mol. Biol.* **1996**, *260*, 126−134.
(37) Chiu, T. K.; Kubelka, J.; Herbst-Irmer, R.; Eaton, W. A.; Hofrichter, J.; Davies, D. R. High-Resolution X-Ray Crystal Structures of the Villin Headpiece Subdomain, an Ultrafast Folding Protein. *Proc. Natl. Acad. Sci. U.S.A.* **2005**, *102*, 7517−7522.
(38) McKnight, C. J.; Matsudaira, P. T.; Kim, P. S. NMR Structure of the 35-Residue Villin Headpiece Subdomain. *Nat. Struct. Biol.* **1997**, *4*, 180−184.
(39) Harrison, R. S.; Sharpe, P. C.; Singh, Y.; Fairlie, D. P. Amyloid Peptides and Proteins in Review. *Rev. Physiol., Biochem. Pharmacol.* **2007**, *159*, 1−77.
(40) Paravastu, A. K.; Qahwash, I.; Leapman, R. D.; Meredith, S. C.; Tycko, R. Seeded growth of -amyloid fibrils from Alzheimer's brain-derived fibrils produces a distinct fibril structure. *Proc. Natl. Acad. Sci. U.S.A.* **2009**, *106*, 7443−7448.
(41) van der Wel, P. C. A. Insights into Protein Misfolding and Aggregation Enabled by Solid-State NMR Spectroscopy. *Solid State Nucl. Magn. Reson.* **2017**, *88*, 1−14.
(42) Wälti, M. A.; Ravotti, F.; Arai, H.; Glabe, C. G.; Wall, J. S.; Böckmann, A.; Güntert, P.; Meier, B. H.; Riek, R. Atomic-resolution structure of a disease-relevant Aβ(1-42) amyloid fibril. *Proc. Natl. Acad. Sci. U.S.A.* **2016**, *113*, E4976−E4984.
(43) Petkova, A. T.; Yau, W.-M.; Tycko, R. Experimental Constraints on Quaternary Structure in Alzheimer's β-Amyloid Fibrils†. *Biochemistry* **2006**, *45*, 498−512.
(44) Panavastu, A.; Leapman, R. D.; Yau, W.-M.; Tycho, R. Molecular Structural Basis for Polymorphism in Alzheimer's β-Amyloid Fibrils. *Proc. Natl. Acad. Sci. U.S.A.* **2008**, *105*, 18349−18354.
(45) McDonald, M.; Box, H.; Bian, W.; Kendall, A.; Tycko, R.; Stubbs, G. Fiber Diffraction Data Indicate a Hollow Core for the Alzheimer's Aβ 3-Fold Symmetric Fibril. *J. Mol. Biol.* **2012**, *423*, 454−461.
(46) Qiang, W.; Yau, W.-M.; Luo, Y.; Mattson, M. P.; Tycko, R. Antiparallel -sheet architecture in Iowa-mutant -amyloid fibrils. *Proc. Natl. Acad. Sci. U.S.A.* **2012**, *109*, 4443−4448.
(47) Rice, D. M.; Wittebort, R. J.; Griffin, R. G.; Meirovitch, E.; Stimson, E. R.; Meinwald, Y. C.; Freed, J. H.; Scheraga, H. A. Rotational jumps of the tyrosine side chain in crystalline enkephalin. Hydrogen-2 NMR line shapes for aromatic ring motions in solids. *J. Am. Chem. Soc.* **1981**, *103*, 7707−7710.
(48) Paluch, P.; Pawlak, T.; Jeziorna, A.; Trébosc, J.; Hou, G.; Vega, A. J.; Amoureux, J.-P.; Dracinsky, M.; Polenova, T.; Potrzebowski, M. J. Analysis of Local Molecular Motions of Aromatic Sidechains in Proteins by 2D and 3D Fast MAS NMR Spectroscopy and Quantum Mechanical Calculations. *Phys. Chem. Chem. Phys.* **2015**, *17*, 28789−28801.
(49) Tugarinov, V.; Liang, Z.; Shapiro, Y. E.; Freed, J. H.; Meirovitch, E. A Structural Mode-Coupling Approach to15N NMR Relaxation in Proteins. *J. Am. Chem. Soc.* **2001**, *123*, 3055−3063.
(50) Miller, Y.; Ma, B.; Nussinov, R. The Unique Alzheimer's β-Amyloid Triangular Fibril Has a Cavity along the Fibril Axis under Physiological Conditions. *J. Am. Chem. Soc.* **2011**, *133*, 2742−2748.
(51) Tchaicheeyan, O.; Freed, J. H.; Meirovitch, E. Local Ordering at Mobile Sites in Proteins from Nuclear Magnetic Resonance Relaxation: The Role of Site Symmetry. *J. Phys. Chem. B* **2016**, *120*, 2886−2898.

DOI: 10.1021/acs.jpcb.8b06330
J. Phys. Chem. B 2018, 122, 8675−8684